

Review

# Additive Manufacturing of Bulk Thermoelectric Architectures: A Review

Cagri Oztan, Ryan Welch and Saniya LeBlanc \* 

Department of Mechanical and Aerospace Engineering, The George Washington University, 800 22nd Street NW, Washington, DC 20052, USA; oztan@gwu.edu (C.O.); welchrj@gwu.edu (R.W.)

\* Correspondence: sleblanc@gwu.edu

**Abstract:** Additive manufacturing offers several opportunities for thermoelectric energy harvesting systems. This new manufacturing approach enables customized leg geometries, minimized thermal boundary resistances, less retooling, reduced thermoelectric material waste, and strong potential to manipulate microstructure for higher values of figure of merit. Although additive manufacturing has been used to fabricate thin thermoelectric films, there has been comparatively limited demonstrations of additive manufacturing for bulk thermoelectric structures. This review provides insights about the current progress of bulk thermoelectric material and device additive manufacturing. Each additive manufacturing technique used to produce bulk thermoelectric structures is discussed in detail along with future directions and challenges.

**Keywords:** thermoelectrics; additive manufacturing; energy conversion

## 1. Introduction

Thermoelectric (TE) devices are solid-state, semiconductor devices in which an electric potential results from the presence of a temperature difference or vice versa [1]. Thus, they are an attractive option for waste heat recovery (direct heat to electricity conversion) and localized thermal management. However, TE devices have failed to find a foothold in prolific applications and markets. Their conversion efficiencies are low (~5%), and they are not easily integrated into other systems. Thus, it is challenging for TE devices to be a viable, cost-effective solution for distributed power generation or thermal management. Additive manufacturing of thermoelectric devices offers the potential to improve thermoelectric device efficiencies as well as enable integration of thermoelectric conversion into other materials and systems.

A conventional TE module consists of p- and n-type semiconductor legs connected thermally in parallel and electrically in series. TE materials are made of inorganic semiconductors such as skutterudites [2], chalcogenides [3], half-Heusler alloys [4], oxides [5–7] or conductive organic polymers like polypyrrole (PPy) [8], polyaniline (PANI) [9], and poly(3,4-ethylenedioxythiophene) (PEDOT) [10]. The efficiency of a TE material is governed by dimensionless figure of merit,  $ZT$ , which is defined in Equation (1):

$$ZT = \frac{S^2\sigma}{k}T \quad (1)$$

where  $S$ ,  $\sigma$ ,  $T$  and  $k$  denote Seebeck coefficient, electrical conductivity, absolute temperature, and thermal conductivity, respectively [11]. For a TE material to be considered efficient, high power factor ( $S^2\sigma$ ) and low thermal conductivity must be achieved at a certain temperature.

In traditional fabrication of TE devices, high-energy techniques such as melt spinning [12], spark plasma sintering [13], arc melting [14], and ball-milling [15] are commonly used. The resultant ingots are diced into legs, which are subsequently assembled between metal contacts on ceramic substrates [16]. However, traditional fabrication techniques are



**Citation:** Oztan, C.; Welch, R.; LeBlanc, S. Additive Manufacturing of Bulk Thermoelectric Architectures: A Review. *Energies* **2022**, *15*, 3121. <https://doi.org/10.3390/en15093121>

Academic Editor: Bertrand Lenoir

Received: 2 March 2022

Accepted: 18 April 2022

Published: 25 April 2022

**Publisher's Note:** MDPI stays neutral with regard to jurisdictional claims in published maps and institutional affiliations.



**Copyright:** © 2022 by the authors. Licensee MDPI, Basel, Switzerland. This article is an open access article distributed under the terms and conditions of the Creative Commons Attribution (CC BY) license (<https://creativecommons.org/licenses/by/4.0/>).

laborious and require use of expensive equipment. A substantial amount of the TE material is wasted, especially during the dicing step [17]. Moreover, such techniques only allow planar form factors (i.e., only thin, flat devices) which hinders efficient heat transfer on non-planar surfaces because the high thermal boundary resistance is high as shown in Figure 1. Hence, a fabrication process that renders conformal geometries or better system integration would be transformative [18–20]. Additive manufacturing (AM) has emerged as a promising alternative.

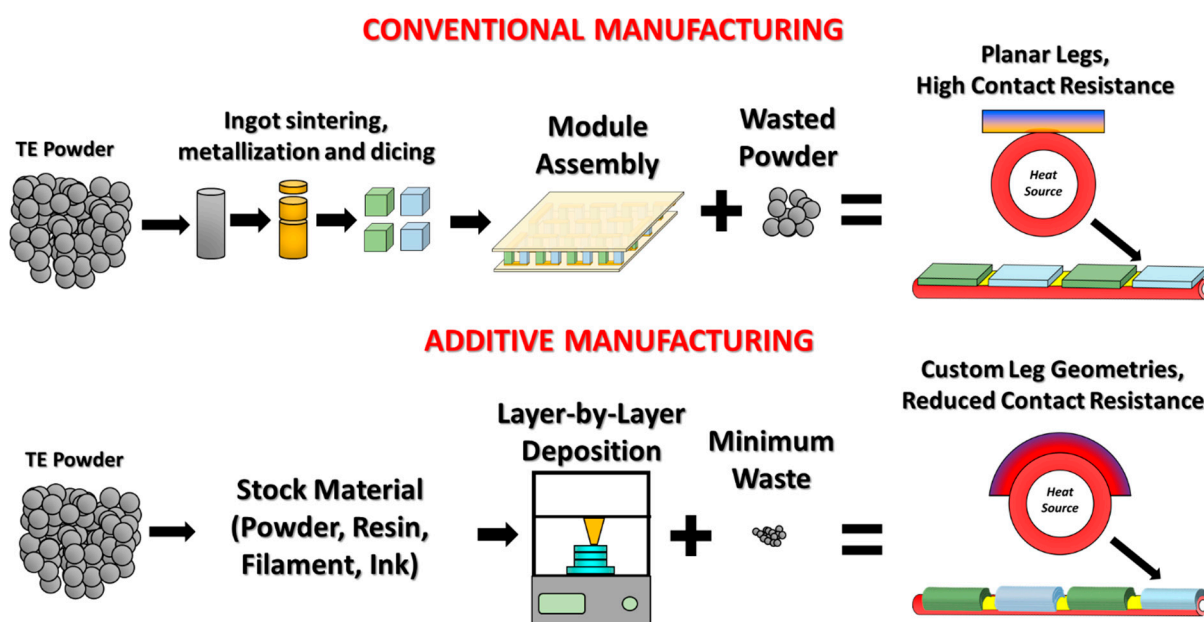


Figure 1. Comparison of additive and conventional manufacturing for TE materials.

Additive manufacturing (AM), conventionally called 3D printing, is a way of rapid prototyping complex geometries that are otherwise difficult to fabricate via conventional methods [21]. It involves deposition of the feedstock material in a layer-by-layer fashion with process parameters dictated by a computer-controlled algorithm. AM has been demonstrated as more straightforward, versatile, flexible, and rapidly deployable than traditional fabrication techniques owing to its minimized need for retooling, negligible waste, and feasibility for a diverse range of materials [22,23]. According to the corresponding standard by International Organization for Standardization/American Society for Testing and Materials (ISO/ASTM 52900:2015), AM methods are classified into seven sub-categories: material extrusion, material jetting, powder bed fusion, vat photopolymerization, binder jetting, direct energy deposition, and sheet lamination as summarized in Table 1 [24].

Table 1. Classification of AM methods material extrusion, material jetting, powder bed fusion, vat photopolymerization, binder jetting, direct energy deposition, and sheet lamination as per ISO/ASTM 52900:2015.

Method	Used for	Principle	Advantages	Disadvantages	Ref	Highest ZT Reported
Material Extrusion	Composites, Polymers, Ceramics	Deposition through a nozzle in filament/ink form	Widespread, inexpensive, adaptable	Anisotropy, High Surface Roughness, Low resolution	[25]	1.7 at 485 °C [26]
Vat Photopolymerization	Polymers, Ceramics	Photocuring of the resin material	High resolution, excellent surface finish	Support structure needed, post-processing required, poor strength.	[27]	1.0 at 27 °C [28]

Table 1. Cont.

Method	Used for	Principle	Advantages	Disadvantages	Ref	Highest ZT Reported
Powder Bed Fusion	Metals, Polymers, Ceramics, Composites	Fusion of powders via a high energy beam	High resolution, wide range of printable materials	High investment cost, size limitations	[29]	1.29 at 50 °C [30]
Binder Jetting	Metals, Polymers, Ceramics, Composites	Selective deposition of a binding agent onto powder layers	Low cost, high speed	Poor strength, post-processing needed	[31]	N/A
Material Jetting	Polymers, Ceramics, Composites	Layer-by-layer solidification of droplets deposited using a dispenser	High accuracy, low waste, multi-material	Support material needed	[32]	N/A
Sheet Lamination	Polymers, Metals, Ceramics	Consolidation of sheet layers into bulk structures	High speed, low cost	Post-processing needed	[32]	N/A
Direct Energy Deposition	Metals	Beam/Arc melting of a material deposited through a high degree of freedom nozzle in powder/wire form	High processing rate, large parts manufacturable	Coarse surface finish	[33]	N/A

## 2. Additively Manufactured Bulk TE Structures

The AM techniques used for fabrication of bulk TE structures with thicknesses in the millimeter range are material extrusion, laser powder bed fusion, and vat photopolymerization. Material and binder jetting have been used to make thin film TEs, as well. Excellent reviews about printed thin films with sub-millimeter thickness [34–36]; this review discusses only printed bulk TE architectures.

### 2.1. Material Extrusion

Among all AM methods, material extrusion is the most commonly used since it is inexpensive and allows fabrication of a wide range of materials such as composites, ceramics, and polymers [21] (pp. 23–51). Material extrusion relies on deposition of a material in a filament or viscous ink form onto a substrate which may be maintained at a certain temperature (Figure 2A). As an inexpensive method that enables extrusion of multiple materials, material extrusion is suitable for printing fully functional materials with anisotropic properties [37]. Depending on to the material extruded, the method is commercially licensed as fused deposition modeling (FDM), fused filament fabrication (FFF) and direct ink writing (DIW) [38].

Material extrusion requires organic or inorganic binders as rheological modifiers to ensure stable deposition. In solid filament-based material extrusion of TE bulk structures, only organic polymeric binders have been employed so far. The first attempt was by Wang et al. where they tailored TE and mechanical properties of PLA (Polylactic Acid)/BST ( $\text{Bi}_{0.5}\text{Sb}_{1.5}\text{Te}_3$ ) composite filaments at varying loadings of multi-walled carbon nanotubes (MWCNTs), silane coupling agent and plasticizer. Although a functional bulk TE sample was not fabricated, the filament with the  $\text{Bi}_{0.5}\text{Sb}_{1.5}\text{Te}_3$ /MWCNTs weight ratio of 81.3/4% resulted in a ZT of 0.011 at room temperature [39]. In this regard, Wang et al.'s strategy was later used by Oztan et al. to fabricate bulk, p-type bismuth telluride ( $\text{Bi}_2\text{Te}_3$ ) structures. Bulk cubes with an edge of 1 mm were fabricated with 20 wt% organic acrylonitrile-butadiene-styrene (ABS) used as a binding agent. Heat treatment at 450, 500, 550 and 575 °C was done to decompose the ABS matrix, resulting in a noteworthy enhancement in TE properties, albeit with a reduction in the strength. The bulk cubes sintered at 500 °C exhibited a

maximum  $ZT$  of 0.54 at room temperature [40]. Aw et al. also used material extrusion to fabricate conductive ABS/Zinc Oxide (ABS/ZnO) composites with various infill ratios and patterns. The samples with 100% rectilinear infill pattern possessed the highest  $ZT$  of  $5.7 \times 10^{-5}$  at room temperature [41].

Rheological modification of inks using organic binders is less laborious than fabrication of filaments with a homogeneously distributed organic binder matrix. While they have low thermal conductivity, organic materials also suffer from low electrical conductivity [42]. To overcome this limitation, Kim et al. reported a ground-breaking study where all-inorganic viscoelastic TE inks with  $\text{Sb}_2\text{Te}_3$  chalcogenidometallate (ChaM) ions as inorganic binders for  $\text{Bi}_2\text{Te}_3$ -based particles were used [43]. Bulk cuboid, disc and half-ring samples were fabricated and characterized; maximum  $ZT$  values of 0.9 at 125 °C and 0.6 at 175 °C for p- and n-type samples, respectively, were achieved. These superior numbers were attributed to the transition of the highly soluble ChaM ions into crystalline semiconducting metal chalcogenides after heat treatment. The authors also successfully printed a functional, conformal TE device for power generation on an alumina pipe where a 2.3–5.2 times larger output voltage per TE couple and up to an order of magnitude larger output power than the planar TE generators were reported. Similar to Kim et al.'s work, inorganic ink-based material extrusion of functional tubular TE generators for high temperature applications was demonstrated by Lee et al. The doping-induced surface charges of PbTe particles were exploited to improve the viscoelasticity of the ink. The impurity-free PbTe ink was a suitable material for fabrication of substrate-free, self-sustaining structures. Bulk legs with various shapes such as cuboid, cylinder, plate, disk, perforated plate, and tube were later sintered without considerable loss in mechanical properties. Printed p- and n-type bulk legs demonstrated maximum  $ZT$  values of 1.6 and 1.4 at 477 °C [44]. The high- $ZT$  tubular device yielded a maximum power density of 153.7 m-W/cm<sup>2</sup>, outpacing Kim et al.'s work [43]. As with filament-based material extrusion, ink-based material extrusion enables multi-material deposition [45]. A multi-material approach based on all-inorganic TE ink containing  $\text{Bi}_x\text{Sb}_{2-x}\text{Te}_3$  particles ( $x = 0.3\text{--}0.6$ ) and ChaM was reported by Yang et al. where they successfully fabricated compositionally segmented bulk, tri-block TE cuboid legs with a high efficiency of 8.7% under a 236 °C [46].

Topology optimization of printed bulk TE legs using material extrusion with all-inorganic inks has also been reported. Choo et al. investigated  $\text{Cu}_2\text{Se}$  with inorganic, electroviscous  $\text{Se}_8^{2-}$  polyanion inks to print optimized bulk legs with superior power output and mechanical stiffness. Hollow hexagonal column and honeycomb shaped bulk TE architectures demonstrated  $ZT$ s as high as 1.21 at 727 °C owing to the  $\text{Se}_8^{2-}$  polyanions acting as a sintering promoting aid. Moreover, an improvement between 20–25% in power density was observed in the customized legs compared to the cuboid ones, which was also confirmed with simulation [47].

Aside from inorganic binders, a considerable amount of work uses ink-based material extrusion with organic binders. Organic ink binder materials are less expensive and more readily available than their inorganic counterparts. As with the filament-based material extrusion with organic binders, an additional heat treatment step is required to decompose the binder which causes porosity and reduces the electrical conductivity. One example is bulk SnSe TE elements with organic carboxymethylcellulose (CMC) binder; the parts were manufactured via a pseudo material extrusion method devised by Burton et al., where the inks were deposited into sacrificial 3D printed ABS scaffolds. After curing at 600 °C, the 1 mm × 1 mm × 2 mm sized bulk legs fabricated with 4 wt% CMC had a record high  $ZT$  of 1.7 at 485 °C. Moreover, a fully functional module capable of producing 20 μW at 500 °C was demonstrated. The same research group later used a similar strategy on  $\text{Cu}_{2-x}\text{Se}$  ( $x = 0, 0.02, 0.03$ ), a high temperature TE material, to fabricate bulk legs that demonstrated a peak  $ZT$  of  $0.63 \pm 0.09$  at 693 °C [26]. In addition to CMC, various water-soluble organic polymers have been suggested as promising binders due to their excellent viscoelasticity and non-toxicity [35,48–50]. Su et al. reported material extrusion of bulk TE in-plane and annular legs using  $\text{Bi}_2\text{Te}_3/\text{PVP}$  and  $\text{Bi}_{0.5}\text{Sb}_{1.5}\text{Te}_3/\text{PVP}$  slurries in various

concentrations. The assembled tubular TE generator for power generation demonstrated a maximum power output of 0.68 mW, and the n- and p-type legs exhibited maximum ZTs of 0.11 and 0.104, respectively. The results were further corroborated via simulation [51]. In another investigation, an unorthodox ink-based material extrusion method was employed for fabrication of bulk  $\text{Bi}_2\text{Te}_3$  architectures by Kenel et al. The heat treatment step was used for reduction of extruded  $\text{Bi}_2\text{O}_3 + \text{TeO}_2 + \text{Poly-lactic-co-glycolic acid (PLGA)}$  ink to TE  $\text{Bi}_2\text{Te}_3$ . Despite warping and shrinkage, the printed samples were sufficiently self-sustaining and achieved a fairly high ZT of 0.4 [52]. Figure 2 summarizes the operation principle of material extrusion and shows bulk TE samples produced therewith.

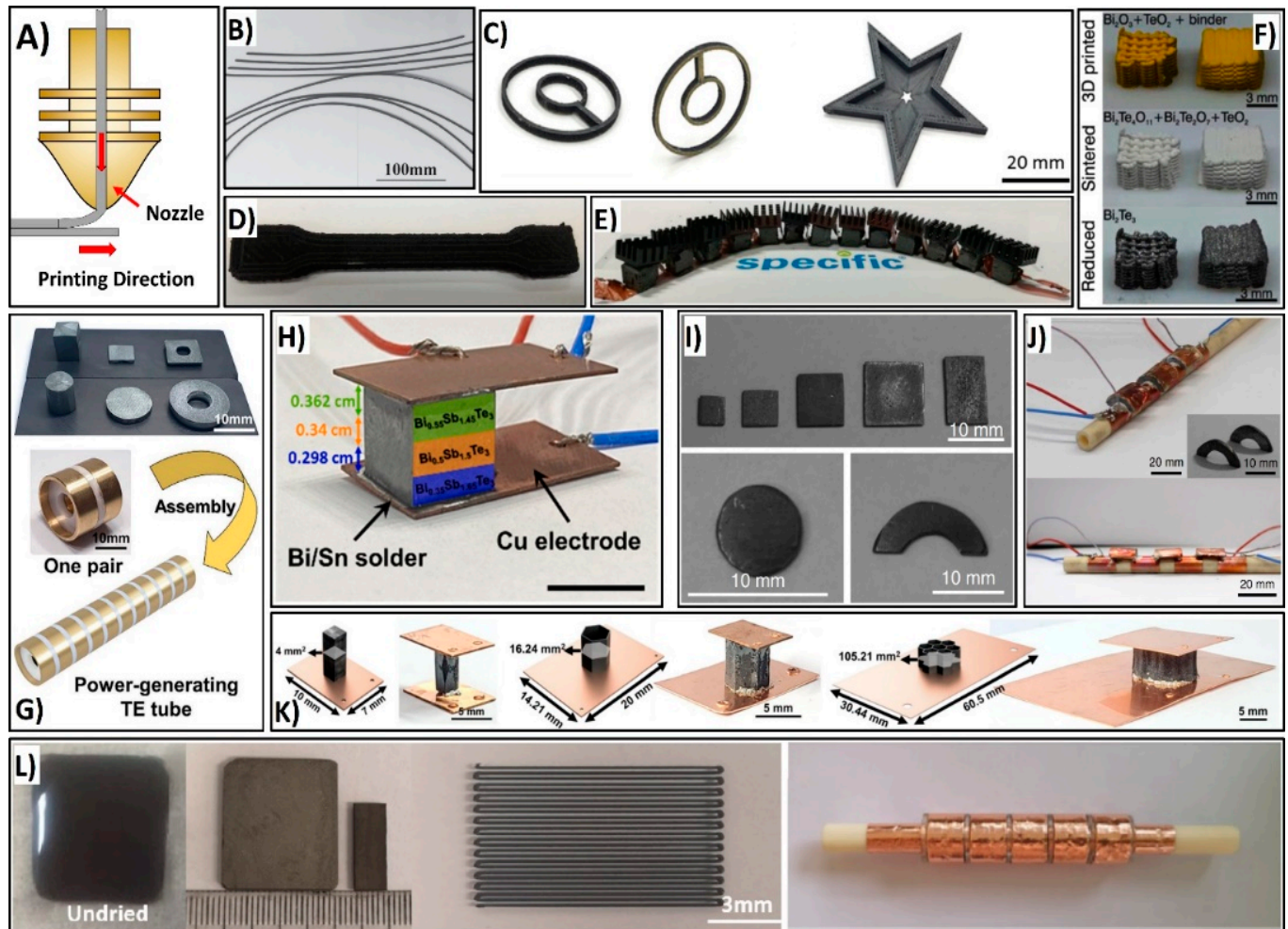


**Figure 2.** (A) Schematic of the working principle of material extrusion, (B)  $\text{Bi}_{0.5}\text{Sb}_{1.5}\text{Te}_3/\text{MWCNT}$  based composite filaments (Reprinted with permission from [39] Wang et al.), (C) Custom printed  $\text{Bi}_2\text{Te}_3$  shapes (Reprinted with permission from [40] Oztan et al.), (D) ABS/ZnO composite sample by Aw et al. [41], (E) SnSe based TE generator by Burton et al. [26], (F) Bulk  $\text{Bi}_2\text{Te}_3$  scaffolds (Reprinted with permission from [52]. 2021, Kenel et al.), (G) Bulk PbTe samples in various shapes and the resultant functional TE generator by Lee et al. [44] (H) Composition-segmented BiSbTe generator (Reprinted with permission from [46]. 2021, Yang et al.), (I, J) Bulk samples and the tubular TE generator printed using all-inorganic  $\text{Bi}_2\text{Te}_3 + \text{Sb}_2\text{Te}_3$  ChaM inks (Reprinted with permission from [43]. 2018, Kim et al.), (K) Cuboid, hollow hexagonal column, and honeycomb-shaped printed bulk  $\text{Cu}_2\text{Se}$  TE legs by Choo et al. [47], (L) As-printed and sintered bulk samples and the tubular TE generator based on  $\text{Bi}_2\text{Te}_3/\text{PVP-Bi}_{0.5}\text{Sb}_{1.5}\text{Te}_3/\text{PVP}$  inks (Reprinted with permission from [51]. 2020, Su et al.).

As the most commonly used AM method, material extrusion is applicable to a broad range of materials due to its scalable, adaptable, cost-effective, straightforward, and versatile features. Various organic, inorganic and hybrid composite TE ink and filament formulations have been devised so far. While filament-based material extrusion methods enable fabrication of TE elements with considerably high strength, the need for a heat treatment step to decompose the binder impacts the phase purity. Similar to its filament-based counterpart, ink-based material extrusion requires a heat treatment step to cure the ink and improve the part strength. In both methods, this heat treatment step induces porosity in the microstructure, reducing the electrical conductivity and leading to lower  $ZT$ s than the bulk counterparts. The heat treatment step also causes warping, shrinkage, and other geometric inconsistencies in the legs, which arguably is the most severe drawback of the method. For all these reasons, careful selection of the process parameters in the heat treatment step is imperative. On the other hand, with the trailblazing introduction of ChaM as an inorganic binder with excellent electrical and rheological properties, material extrusion has evolved into a technique that offers ample opportunities for AM of bulk TE architectures. Considering many of the TE waste heat recovery applications require TE devices to operate on curved surfaces [53–56], material extrusion using all-inorganic inks can be an excellent candidate to enable in-situ TE generator fabrication on such surfaces.

## 2.2. Vat Photopolymerization

Vat photopolymerization is another common additive manufacturing technique that involves consolidation of a photocurable polymer resin by a light source in a selective and layer-by-layer fashion [57]. The technique is patented under the monikers Stereolithography (SLA), Digital Light Processing (DLP), and Continuous Liquid Interface Production (CLIP), depending on the source and direction of the light used [58].

From a TE fabrication perspective, vat photopolymerization has limited interest so far. The first attempt was made by He et al. in 2015 to fabricate p-type amorphous  $\text{Bi}_{0.5}\text{Sb}_{1.5}\text{Te}_3$  bulk samples with ultralow thermal conductivity. The composite resins were loaded with 40–60 wt%  $\text{Bi}_{0.5}\text{Sb}_{1.5}\text{Te}_3$  and processed under a 405 nm laser beam at a laser power of 1.2 W and layer height of 100  $\mu\text{m}$ . A post-processing step with parameters optimized via thermogravimetric analysis (TGA) was applied to decompose the residual resin and enhance the electrical conductivity. Despite the resultant ultralow thermal conductivity of 0.2 W/m-K, the remaining porosity caused a low electrical conductivity and led to a maximum  $ZT$  of 0.12 at room temperature [59]. Vat photopolymerization was later used by Park et al. for fabrication of bulk TE elements with orthorhombic  $\beta\text{-Ag}_2\text{Se}$  phase, a TE compound for room temperature applications [60–62]. The bulk samples with various ratios of  $\beta\text{-Ag}_2\text{Se}$  were fabricated and characterized for tensile strength and TE properties. Despite an approximate loss by 55% in tensile strength, the samples loaded with 30 wt%  $\beta\text{-Ag}_2\text{Se}$  exhibited a maximum  $ZT$  of 0.12 at 27 °C. A quasi-printing technique using vat photopolymerization for bulk TE fabrication was reported by Mallick et al. In this method, n-type  $\beta\text{-Ag}_2\text{Se}$  and p-type PEDOT inks were painted on vat photopolymerization printed scaffolds with three distinct geometries for topology optimization [28]. N-type  $\beta\text{-Ag}_2\text{Se}$  yielded a maximum  $ZT$  of 1.0 in the room temperature, and a maximum output power of 7  $\mu\text{W}$  was observed in cylindrical bulk legs.

Although the vat photopolymerization technique offers excellent surface finish and high resolution, it has numerous hurdles such as limited photopolymerizable resins [63] and a requisite post-curing process to eliminate the binder in the resin as with material extrusion. The samples fabricated by this method exhibited significantly lower  $ZT$ s than their traditionally manufactured bulk counterparts. A summary of the use of vat photopolymerization bulk TE fabrication is provided in Figure 3.

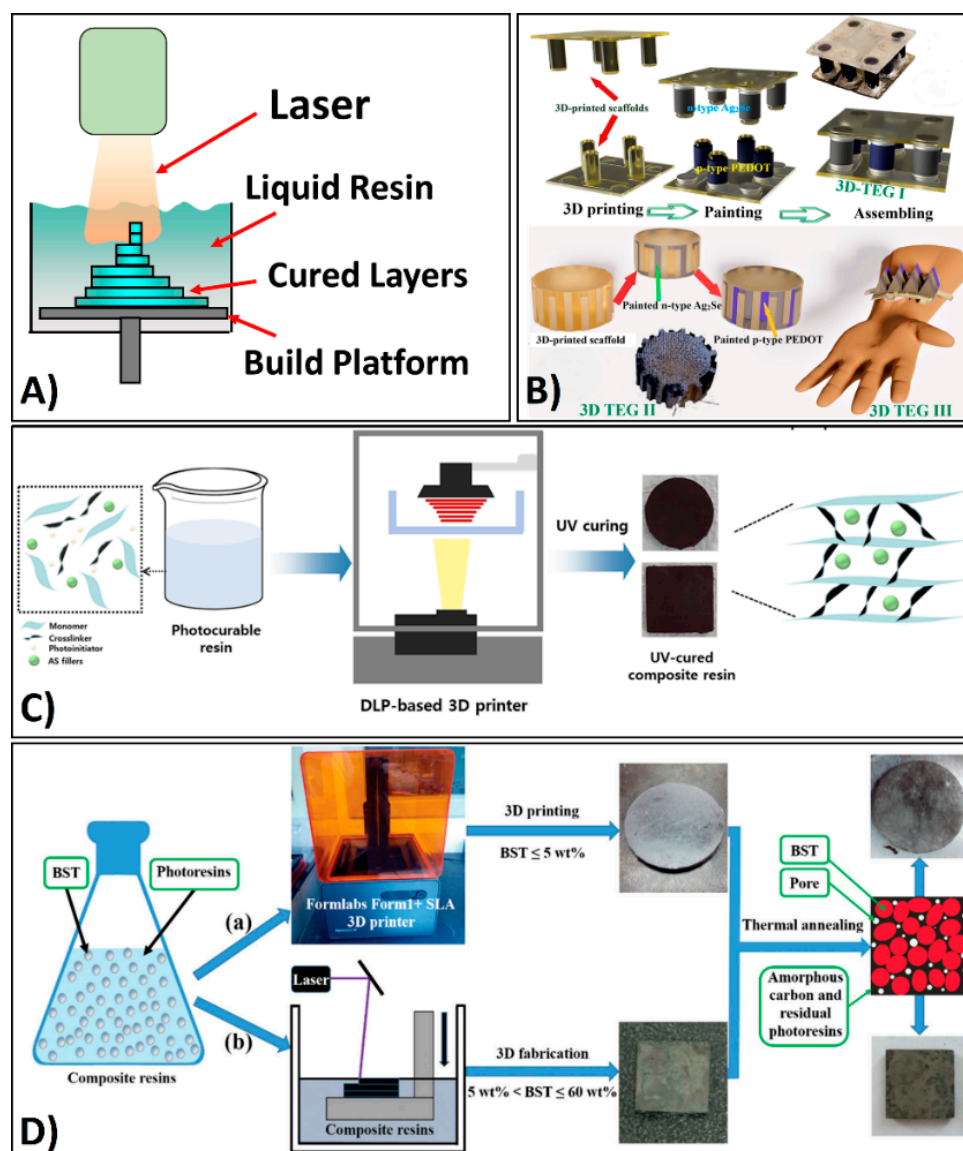


**Figure 3.** (A) Working principle of vat photopolymerization, (B) Quasi-vat photopolymerization printed  $\beta$ - $\text{Ag}_2\text{Se}$ -PEDOT TE generators fabricated by Mallick et al. [28], (C) Bulk  $\beta$ - $\text{Ag}_2\text{Se}$  TE structures made by Park et al. [62], (D) Bulk  $\text{Bi}_{0.5}\text{Sb}_{1.5}\text{Te}_3$  samples made by He et al. [59] (*Reproduced with permission*).

### 2.3. Powder Bed Fusion

Powder bed fusion utilizes a laser or electron beam as an energy source to enable localized melting of a powder material followed by solidification in a layer-by-layer fashion. The method is versatile because it allows fabrication of highly dense metal, composite, ceramic, and polymeric parts with small-to-medium size and customized shapes [64–66]. Powder bed fusion is classified into several sub-categories such as Selective Laser Sintering (SLS), Direct Metal Laser Sintering (DMLS), and Electron Beam Melting (EBM) [67]. In powder bed fusion, as the beam interacts with the material, a melt pool forms and solidifies with a unique microstructure comprised of preferential grain alignment along the direction of the thermal gradient, resulting in anisotropic properties [68]. Powder bed fusion involves a complex combination of multiple physics such as conductive, radiative, and convective heat transfer, surface tension driven mass transport and thermo-capillary convection [69]. Hence, a comprehensive understanding of this process is still a major goal in the field of AM. Certain dimensionless numbers that are commonly used in fluid mechanics and heat

transfer such as normalized enthalpy, Marangoni number, Fourier number and Peclet number [70,71] have enabled more precise understanding of the physics involved in the process, and a commonly used process parameter to predict the microstructure is the volumetric energy density ( $E_v$ ) given in Equation (2):

$$E_v = \frac{P}{vhd} \quad (2)$$

where  $P$ ,  $v$ ,  $h$ , and  $d$  are the beam power, scan speed, hatch spacing, and layer thickness, respectively. Sometimes, Equation (2) is used without the  $d$  or without both the  $d$  and  $h$  terms to denote surface energy density ( $E_s$ ) or linear energy density ( $E_l$ ), respectively.

While AM of bulk TE structures via powder bed fusion is a rather new concept, it has attracted significant attention. The main advantage of using powder bed fusion is the potential to create hierarchical structuring. The technique can be used to introduce inclusions and grain boundaries [72] that lead to increased phonon scattering for lower thermal conductivity and increased charge carrier energy filters for enhanced Seebeck coefficient simultaneously [73]. This AM approach can also enable meso-/macro-scale topological design and optimization for system-level benefits.

Prior to achieving the fabrication of a bulk TE sample via powder bed fusion, noteworthy investigations were performed on  $\text{Bi}_2\text{Te}_3$  using single melt lines on powder compacts to determine the optimum process parameters. The first published attempt was made by Read et al. using an Nd: YLF pulse laser setup. Under a laser spot size of 173  $\mu\text{m}$  and varying laser powers and scan speeds between 0.5–2 W and 5–40 mm/s (which corresponded to energy densities of 0.07–1.17 J/mm<sup>2</sup>), formation of stable single melt lines was observed.  $\text{Bi}_2\text{Te}_3$  underwent excessive vaporization at heat fluxes above 33.5 W/mm<sup>2</sup> [74]. Subsequently, these promising results were expanded by El-Desouky et al. using the same Nd: YLF pulse laser setup to optimize the laser spot size. With a larger laser spot size of 300  $\mu\text{m}$  and laser scanning speeds and powers of 1–2 W and 5–20 mm/s (which corresponded to an energy density range of 0.29–1.17 J/mm<sup>2</sup>), minimized ejection of the powder was observed. Excessive material ejection and splatter were reported at a higher energy density of 1.8 J/cm<sup>2</sup> [75]. El-Desouky et al. later observed that under the laser spot size of 300  $\mu\text{m}$ , higher laser powers of 3–5 W led to reduced porosity [76]. In their subsequent research, El-Desouky et al. continued investigating the melt pool and microstructure formation of  $\text{Bi}_2\text{Te}_3$  disks under even higher laser powers and scan speeds (10–25 W and 350 mm/s), yet with similar volumetric energy intensities due to the reduced laser spot size (70  $\mu\text{m}$ ). Imaging revealed increased laser power allowed deeper permeation of the laser heating into the matrix, resulting in higher melt pool depth. On the other hand, increased levels of energy density significantly mitigated the surface porosities, but formation on spherical and irregular subsurface pores persisted due to the trapped gases and shrinkage at the melt pool boundaries. In this research, phase purity, which is primarily governed by the beam parameters and oxidation, was also characterized using X-ray diffraction; no secondary phases were detected [77]. These studies showed  $\text{Bi}_2\text{Te}_3$  was a suitable candidate for powder bed fusion using a single-layer consolidation strategy on compacted  $\text{Bi}_2\text{Te}_3$  disks to explore the process-microstructure relationship.

The first research concerning single-step powder bed fusion manufactured bulk TE structures was reported by Zhang et al. [78] using a continuous wave laser to consolidate undoped  $\text{Bi}_2\text{Te}_3$  powder. Bulk  $\text{Bi}_2\text{Te}_3$  structures over 1 mm thick were fabricated under 16 and 25 W laser power at constant scan speed, hatch space and spot size of 500 mm/s, 37.5  $\mu\text{m}$  and 50  $\mu\text{m}$ , respectively. The powder bed fusion-made bulk samples exhibited no difference in phase purity from their hot-pressed counterparts. At a laser power of 25 W, a maximum  $ZT$  of 0.11 at 50 °C was achieved. The relative density of 88% was attributed to the voids and mechanical interlocking of the  $\text{Bi}_2\text{Te}_3$  powder before melting due to the powder particles' high aspect ratio. Fully powder bed fusion-processed bulk TE samples out of pure powder was reported by Shi et al., as well, where p-type commercial  $\text{Bi}_{0.5}\text{Sb}_{1.5}\text{Te}_3$  powder was laser processed under a constant scan speed of 3200 mm/s, laser power of

30 W and varying hatch spaces of 50  $\mu\text{m}$  and 80  $\mu\text{m}$  [30]. A 12 mm  $\times$  3 mm  $\times$  2 mm square block and cylinder sample with a diameter of 12.7mm and thickness of 2 mm were successfully fabricated. Due to the process-induced artefacts, the samples exhibited a highly porous microstructure with maximum relative densities of 54.3% (50  $\mu\text{m}$  hatch spacing) and 45.5% (80  $\mu\text{m}$  hatch spacing). Although the porosity caused more than a 50% decrease in electrical conductivity compared to the bulk  $\text{Bi}_{0.5}\text{Sb}_{1.5}\text{Te}_3$  alloy, thermal conductivity decreased by more than 75%. Thus, a maximum  $ZT$  of 1.29 at 50  $^\circ\text{C}$  was achieved, which is 40% higher than the bulk  $\text{Bi}_{0.5}\text{Sb}_{1.5}\text{Te}_3$  sample. Welch et al. studied powder bed fusion of n-type  $\text{Bi}_2\text{Te}_{2.7}\text{Se}_{0.3}$  powder synthesized by ball milling. The microstructure and phase purity of a 3 mm thick, laser-consolidated bulk sample were analyzed. Oxidation was observed, likely due to trace oxygen in the processing chamber. The maximum density recorded in this research was 75% due to low powder layer packing density and processing close to the transition threshold between conduction and keyhole mode processing [79]. Welch et al. [80] also studied powder bed fusion of n-type  $\text{Bi}_2\text{Te}_3$  powder using a continuous laser system to explore its process-structure-property relationship. A comprehensive transmission electron microscopy analysis showed the presence of grain boundaries, oxide inclusions, and tellurium deficient regions, the combination of which likely caused a shift in primary charge carrier and resulted in p-type behavior. Other than  $\text{Bi}_2\text{Te}_3$ , Zhang et al. also demonstrated the first laser powder bed fusion of half-Heusler alloys using pure  $\text{ZrNiSn}$  and nano  $\text{ZrO}_2$  doped  $\text{Hf}_{0.3}\text{Zr}_{0.7}\text{CoSn}_{0.3}\text{Sb}_{0.7}$ . The base powders were successfully consolidated into flat disks with a diameter of 8 mm and thickness over 1 mm. Although no TE properties were reported, the produced parts retained most of their original chemical composition with small chemical variations due to the decomposition and oxidation during the interaction of the materials with laser. The results manifested that TE half-Heusler alloys are suitable for powder bed fusion [81].

In all works described so far, powder bed fusion experiments were conducted through deposition of the pre-synthesized TE alloy powder on a build plate. In the innovative approach reported by Gascoin et al., laser based powder bed fusion was exploited to perform the alloying process itself, enabling a less time-consuming fabrication procedure since the TE alloy would be formed at the same time that the part is manufactured. Laser scanned higher manganese silicide (HMS) sheet samples exhibited high phase purity, enabling a potential layer-by-layer fabrication of this material into a bulk sample [82]. This strategy was later employed by Shi et al. where a pseudo-homogeneous mixture of individual elemental powders of Sb and Te were laser scanned twice under 60–100 W laser power and 200–300 mm/s scan speed and 50  $\mu\text{m}$  hatch spacing [83]. X-ray diffraction analysis indicated atomic ratios close to stoichiometry, and the parts had high relative density of 99.91% and a  $ZT$  of 0.4 at 250  $^\circ\text{C}$ .

As with material extrusion, rheological modification of the feedstock material in powder bed fusion is possible with organic binders, surfactants, and solvents for enhanced flowability and mechanical integrity [84,85]. For example, Xiong et al. used E12 epoxy as the binder in n-type  $\text{Bi}_2\text{Te}_3$  powder to fabricate prismatic bulk samples with a diameter of 4 mm  $\times$  4 mm  $\times$  20 mm. Due to its low melting point, good bonding property and minimal heat shrinkage, E12 epoxy was a suitable candidate as a binder. A bulk sample was successfully manufactured with a laser power of 22 W, scan speed of 3000 mm/s and a hatch spacing of 260  $\mu\text{m}$ . Subsequent degassing of the epoxy resulted in a relative density and  $ZT$  of 63.30% and 0.88 (at 77  $^\circ\text{C}$ ), respectively [86]. Figure 4 displays the powder bed fusion manufactured TE samples from select publications.

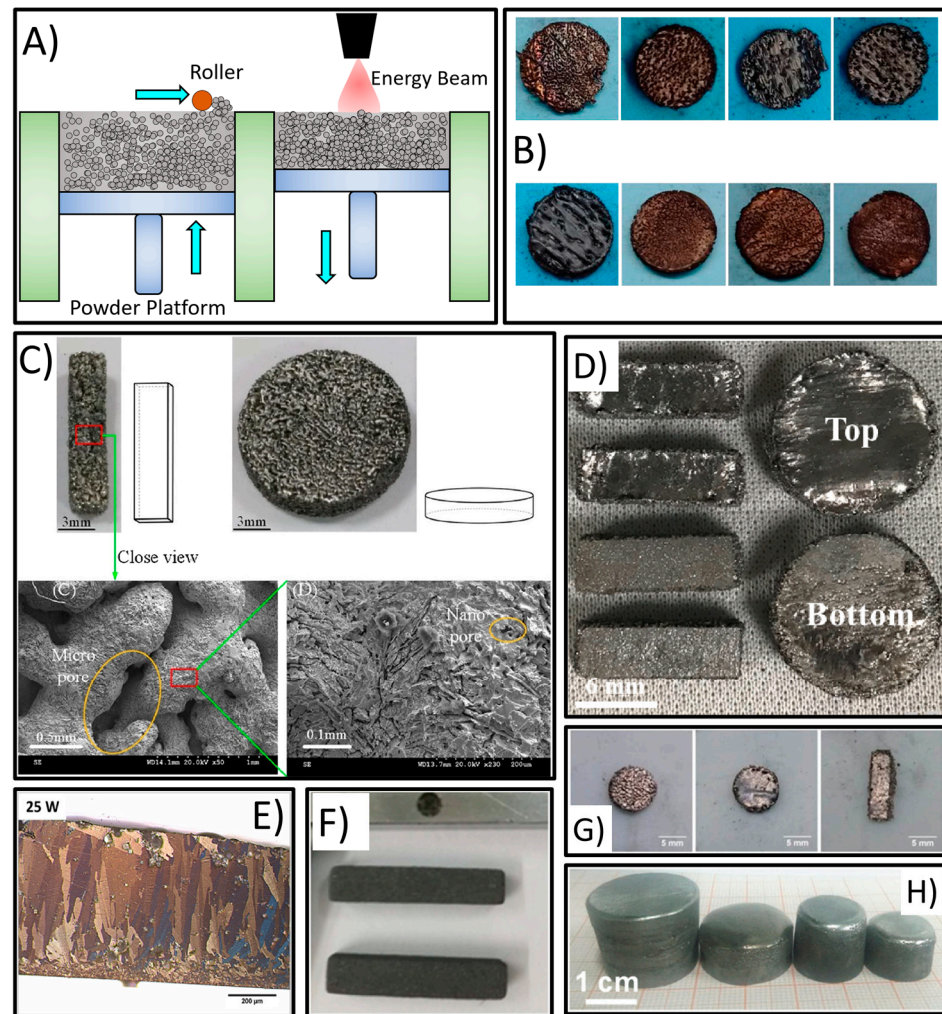


**Figure 4.** (A) Working principle of powder bed fusion, (B) Nano  $ZrO_2$  doped  $Hf_{0.3}Zr_{0.7}CoSn_{0.3}Sb_{0.7}$  bulk disks with a diameter of 8 mm and thickness over 1 mm [81], (C) 2 mm-thick  $Bi_{0.5}Sb_{1.5}Te_3$  parts and their porous microstructure (Reprinted with permission from [30]. 2019, Shi et al.), (D) 1 mm-thick  $Sb_2Te_3$  samples alloyed via powder bed fusion (Reprinted with permission from [83]. 2021, Shi et al.), (E) Preferential grain orientation in powder bed fusion processed  $Bi_2Te_3$  (Reprinted with permission from [77]. 2017, El-desouky et al.), (F) Bulk rectangular prism (4 mm  $\times$  4 mm  $\times$  20 mm) and cylinder (12.7 mm  $\times$  3 mm) samples made via laser powder bed fusion of n-type  $Bi_2Te_3$  samples/epoxy composite powder by Xiong [86], (G) Bulk  $Bi_2Te_3$  samples (Reprinted with permission from [78]. 2018, Zhang et al.), (H) Bulk p-type  $BiSbTe$  samples fabricated (Reprinted with permission from [87]. 2008, Qiu et al.).

Hybrid manufacturing of bulk TE elements involving powder bed fusion has also attracted considerable attention. Wu et al. combined powder bed fusion and ink-based material extrusion to enable multi-material printing for device fabrication [88]. A slurry made of Tween 20, Antifoam AR and n-type  $Bi_2Te_{2.7}Se_{0.3}$  was prepared via high temperature synthesis and ball milling and ink-printed onto a substrate in a drop-on-demand manner. The deposited slurry was later processed by powder bed fusion at 6 W and 80 mm/s. A bulk composite sample with a thickness of 1.5 mm was obtained by consecutively stacking 75 layers of ink-deposited slurry. A maximum  $ZT$  of 0.3 at 177 °C was reported. Due to the presence of the organic additives in the slurry, unidentified peaks in XRD analysis were detected; these peaks were not present after annealing. Mao et al. [89] studied powder bed fusion of n-type  $Bi_2Te_{2.7}Se_{0.3}$  powder deposited on a substrate made of the same material. The laser processing parameters were 4–8 W, 50–200 mm/s and 30–80  $\mu$ m (hatch

spacing) with a powder layer height of 30  $\mu\text{m}$ . Due to the high propensity of Te and Se to evaporate during consolidation, different compositions of  $\text{Bi}_2\text{Te}_{2.7-x}\text{Se}_{0.3-y}$ , ( $0.72 \geq x \geq 0.1$ ,  $0.2 \geq y \geq 0.07$ ) were observed. To mitigate this, a bulk sample with 10 mol% of excess Te was fabricated and characterized for phase purity and TE properties. A bulk composite 1.5 mm thick sample was manufactured under the optimum parameters of 6 W, 200 mm/s, 50  $\mu\text{m}$  and 0.6 J/mm<sup>2</sup> for laser power, scanning speed, hatch distance and energy density, respectively. Subsequent annealing at 400 °C for 24 h was performed to eliminate any residual stress and inhomogeneity. The maximum  $ZT$  was 0.84 at 127 °C.

The same hybrid AM approach was later employed as a post treatment for material extrusion-printed samples by Greifzu et al. [90] to fabricate thin films with both n- and p-type  $\text{Bi}_2\text{Te}_3$ . Considerably higher laser power and scanning speeds of 80–150 W and 2500–5000 mm/s, respectively, were employed under a regular hatch distance range of 0.3–0.5 mm, which corresponded to energy density ranges of 0.025–0.250 J/mm<sup>2</sup> for the n-type  $\text{Bi}_2\text{Te}_3$  and 0.025–0.160 J/mm<sup>2</sup> for the p-type  $\text{Bi}_2\text{Te}_3$ . The p-type material underwent more than 40% enhancement in electrical conductivity from 15 S/cm to 22 S/cm although the n-type material showed a significant reduction from 88 S/cm to 7 S/cm. On the other hand, absolute Seebeck coefficients demonstrated dramatic reductions from 251  $\mu\text{V/K}$  to 40–70  $\mu\text{V/K}$  for the p-type material and from 142  $\mu\text{V/K}$  to 110  $\mu\text{V/K}$  for the n-type material. It was concluded that the design of experiments could not yield optimum parameters due to the inconsistent results. In another hybrid approach combining traditional and additive powder bed fusion technique, Yan et al. [91] laser processed n-type  $\text{CoSb}_{2.85}\text{Te}_{0.15}$  skutterudite and ethanol slurry on a Ti substrate for medium-temperature TE applications. A pulsed fiber laser system was used, and bulk samples with a thickness of 1.7 mm were fabricated by consecutively processing 80 layers at laser parameter of 12–16 W and 50–100 mm/s. The sample was annealed at 450 °C to remove the ethanol from the matrix, resulting in a maximum  $ZT$  of 0.56 at 550 °C. The same hybrid method was also used by Qiu et al. [87] to laser process highly textured p-type  $\text{Bi}_{0.4}\text{Sb}_{1.6}\text{Te}_3$  synthesized via a thermal explosion technique by Yan et al. [92] for n-type  $\text{ZrNiSn}$ , and by Chen et al. for  $\text{SnTe}$  [93].

The key advantage of powder bed fusion for TE over material extrusion techniques is the possibility to make very dense, customized geometries without the need for an additional binder material [94]. Powder bed fusion is also suitable for synthesizing the TE material out of its constituent elements without a significant deviation from stoichiometry of the desired TE alloy [83]. The unique, anisotropic microstructure with preferential grain orientation along the temperature gradient could enable higher Seebeck coefficients and lower thermal conductivity via phonon scattering [80]. However, high temperatures during powder bed fusion may decompose TE materials. Lack of fusion, porosity, thermal cracking, and oxidation are major challenges, and the brittle nature of TE materials [95,96] increases the risk of thermal cracking. Moreover, TE properties are sensitive to any variation in the chemical composition. Hence, the highly complex physics involved in the process require a comprehensive understanding of the process-structure-property relationship. Thus, simulation techniques could reduce the experimental burden and allow prediction of the resultant microstructure [97–104]. The high equipment cost is certainly another major drawback of the method. In conclusion, powder bed fusion of TE structures still needs substantial research and development in order for it to be a viable TE device manufacturing technique.

### 3. Outlook and Future Directions

Thus far, TE energy harvesting on non-planar surfaces has been achieved with flexible thin and thick film TE devices. As an alternative to this, topology optimization of bulk TE legs and devices into customized, shape-conformable geometries has attracted considerable attention. Additive manufacturing provides promising results albeit with limitations in all techniques. In the majority of the material extrusion-based techniques where an organic binder material is used, an additional heat treatment that impedes the TE performance is needed. To overcome this, all-inorganic binders have been developed, which led to record high values of  $ZT$ . On the other hand, powder bed fusion yields parts with hierarchical

structuring and process-dependent microstructures with preferential grain alignment. Such microstructure can enhance  $ZT$  by suppressing thermal conductivity, which is a potential advantage of powder bed fusion over other additive methods. Moreover, powder bed fusion enables binder-free processing of thermoelectric material powder. TE materials typically have lower thermal conductivity and different charge transport mechanisms than the conventional materials used in powder bed fusion, necessitating a more comprehensive understanding of the process-structure-property relationship in powder fusion fabricated TE materials. Finally, despite the high dimensional accuracy of vat polymerization, this technique has attracted less interest than material extrusion and powder bed fusion because there are a limited number of the photocurable resins. Future efforts may be devoted to investigating novel composite resins for vat polymerization of bulk TE structures.

#### 4. Conclusions

Additive manufacturing has recently emerged as an alternative for TE fabrication, with promising results so far. TE energy harvesting on non-planar surfaces has been achieved via AM of flexible thin/thick film TE devices, but topology optimization of bulk TE legs and devices into customized, shape-conformable geometries also offers ample benefits for increases in TE device performance in a broad range of applications. This review discussed the recent progress in additively manufactured bulk thermoelectric structures. Additive manufacturing techniques are adaptable to a wide variety of materials, reduce waste, enable the flexibility to fabricate custom structures, are cost effective, and minimize the need for retooling and post-processing. In conclusion, topologically optimized, additively manufactured bulk TE structures offer an attractive solution for TE energy harvesting and thermal management applications.

**Funding:** This research was funded by U.S. National Science Foundation, Award Number CMMI-1943104 and U.S. Office of Naval Research, Award Number N00014-20-1-2365.

**Acknowledgments:** S.L. gratefully acknowledges support from the National Science Foundation CAREER Award, Award No. CMMI-1943104. S.L. and Y.O. acknowledge support from the Office of Naval Research, Award No. N0014-20-1-2365.

**Conflicts of Interest:** The authors declare no conflict of interest.

#### References

1. Hochbaum, A.I.; Chen, R.; Diaz Delgado, R.; Liang, W.; Garnett, E.C.; Najarian, M.; Majumdar, A.; Yang, P. Enhanced thermoelectric performance of rough silicon nanowires. *Nature* **2008**, *451*, 163–167. [[CrossRef](#)] [[PubMed](#)]
2. Rogl, G.; Rogl, P. Skutterudites, a most promising group of thermoelectric materials. *Curr. Opin. Green Sustain. Chem.* **2017**, *4*, 50–57. [[CrossRef](#)]
3. Shi, Y.; Sturm, C.; Kleinke, H. Chalcogenides as thermoelectric materials. *J. Solid State Chem.* **2019**, *270*, 273–279. [[CrossRef](#)]
4. Bin Masood, K.; Kumar, P.; Singh, R.A.; Singh, J. Odyssey of thermoelectric materials: Foundation of the complex structure. *J. Phys. Commun.* **2018**, *2*, 062001. [[CrossRef](#)]
5. Ren, G.-K.; Wang, S.-Y.; Zhu, Y.-C. Enhancing thermoelectric performance in hierarchically structured BiCuSeO by increasing bond covalency and weakening carrier–phonon coupling. *Energy Environ. Sci.* **2017**, *10*, 1590–1599. [[CrossRef](#)]
6. Ohtaki, M.; Tsubota, T.; Eguchi, K. High-temperature thermoelectric properties of  $(Zn_{1-x}Al_x)O$ . *J. Appl. Phys.* **1996**, *79*, 1816–1818. [[CrossRef](#)]
7. Tan, X.; Liu, Y.C.; Liu, R. Synergistical Enhancement of Thermoelectric Properties in n-Type  $Bi_2O_2$  Se by Carrier Engineering and Hierarchical Microstructure. *Adv. Energy Mater.* **2019**, *9*, 1900354. [[CrossRef](#)]
8. Kemp, N.T.; Kaiser, A.B.; Liu, C.-J. Thermoelectric power and conductivity of different types of polypyrrole. *J. Polym. Sci. Part B Polym. Phys.* **1999**, *37*, 953–960. [[CrossRef](#)]
9. Liu, S.; Li, H.; Li, P.; Liu, Y.; He, C. Recent Advances in Polyaniline-Based Thermoelectric Composites. *CCS Chem.* **2021**, *3*, 2547–2560. [[CrossRef](#)]
10. Liang, L.; Fan, J.; Wang, M.; Chen, G.; Sun, G. Ternary thermoelectric composites of polypyrrole/PEDOT:PSS/carbon nanotube with unique layered structure prepared by one-dimensional polymer nanostructure as template. *Compos. Sci. Technol.* **2020**, *187*, 107948. [[CrossRef](#)]
11. Nolas, G.S.; Sharp, J.; Goldsmid, J. *Thermoelectrics: Basic Principles and New Materials Developments*; Springer Science & Business Media: Berlin/Heidelberg, Germany, 2013; Volume 45.

12. Tkatch, V.I.; Limanovskii, A.I.; Denisenko, S.N.; Rassolov, S.G. The effect of the melt-spinning processing parameters on the rate of cooling. *Mater. Sci. Eng. A* **2002**, *323*, 91–96. [[CrossRef](#)]
13. Kim, J.; Duy, L.T.; Ahn, B.; Seo, H. Pre-oxidation effects on properties of bismuth telluride thermoelectric composites compacted by spark plasma sintering. *J. Asian Ceram. Soc.* **2020**, *8*, 211–221. [[CrossRef](#)]
14. Nataraj, D.; Nagao, J.; Ferhat, M. High temperature thermoelectric properties of arc-melted Ba/sub 8/M/sub 16/Si/sub 30/(M = Al, Ga) clathrates. In *Proceedings of the Twenty-First International Conference on Thermoelectrics, 2002, Proceedings ICT'02, Long Beach, CA, USA, 29 August 2002*; IEEE: Piscataway, NJ, USA, 2002; pp. 72–75.
15. Im, H.J.; Koo, B.; Kim, M.-S.; Lee, J.E. Optimization of high-energy ball milling process for uniform p-type Bi-Sb-Te thermoelectric material powder. *Korean J. Chem. Eng.* **2022**, 1–5. [[CrossRef](#)]
16. Jaziri, N.; Boughamoura, A.; Müller, J.; Mezghani, B.; Tounsi, F.; Ismail, M. A comprehensive review of Thermoelectric Generators: Technologies and common applications. *Energy Rep.* **2019**, *6*, 264–287. [[CrossRef](#)]
17. Cleary, M. Nanostructured High Temperature Bulk Thermoelectric Energy Conversion for Efficient Waste Heat Recovery. In *Proceedings of the Annual Merit Review and Peer Evaluation Meeting, Arlington, Virginia, 8–12 June 2014*.
18. Du, Y.; Chen, J.; Meng, Q.; Dou, Y.; Xu, J.; Shen, S.Z. Thermoelectric materials and devices fabricated by additive manufacturing. *Vacuum* **2020**, *178*, 109384. [[CrossRef](#)]
19. Şişik, B.; Leblanc, S. The Influence of Leg Shape on Thermoelectric Performance Under Constant Temperature and Heat Flux Boundary Conditions. *Front. Mater.* **2020**, *7*, 595955. [[CrossRef](#)]
20. Yang, S.; Gao, Z.; Qiu, P. Ductile Ag<sub>20</sub>S<sub>7</sub>Te<sub>3</sub> with Excellent Shape-Conformability and High Thermoelectric Performance. *Adv. Mater.* **2021**, *33*, 2007681. [[CrossRef](#)]
21. Gibson, I.; Rosen, D.; Stucker, B. *Additive Manufacturing Technologies*; Springer: Berlin/Heidelberg, Germany, 2021; Volume 17.
22. Sun, C.; Wang, Y.; McMurtrey, M.D. Additive manufacturing for energy: A review. *Appl. Energy* **2020**, *282*, 116041. [[CrossRef](#)]
23. Ngo, T.D.; Kashani, A.; Imbalzano, G. Additive manufacturing (3D printing): A review of materials, methods, applications and challenges. *Compos. Part B Eng.* **2018**, *143*, 172–196. [[CrossRef](#)]
24. *F2792-12a*; Standard Terminology for Additive Manufacturing Technologies. ASTM International: West Conshohocken, PA, USA, 2012.
25. Kulkarni, A.; Sorarù, G.D.; Pearce, J.M. Polymer-derived SiOC replica of material extrusion-based 3-D printed plastics. *Addit. Manuf.* **2019**, *32*, 100988. [[CrossRef](#)]
26. Burton, M.R.; Mehraban, S.; Beynon, D.; McGettrick, J.; Watson, T.; Lavery, N.P.; Carnie, M.J. 3D Printed SnSe Thermoelectric Generators with High Figure of Merit. *Adv. Energy Mater.* **2019**, *9*, 1900201. [[CrossRef](#)]
27. Kumaresan, R.; Samykano, M.; Kadirgama, K. 3D Printing Technology for Thermal Application: A Brief Review. *J. Adv. Res. Fluid Mech. Therm. Sci.* **2021**, *83*, 84–97. [[CrossRef](#)]
28. Mallick, M.; Franke, L.; Rösch, A.G.; Lemmer, U. Shape-Versatile 3D Thermoelectric Generators by Additive Manufacturing. *ACS Energy Lett.* **2020**, *6*, 85–91. [[CrossRef](#)]
29. Riabov, D. *The Effects of Morphology and Surface Oxidation of Stainless Steel Powder in Laser Based-Powder Bed Fusion*; Chalmers University of Technology: Göteborg, Sweden, 2020.
30. Shi, J.; Chen, H.; Jia, S.; Wang, W. 3D printing fabrication of porous bismuth antimony telluride and study of the thermoelectric properties. *J. Manuf. Process.* **2018**, *37*, 370–375. [[CrossRef](#)]
31. Salmi, M. Additive Manufacturing Processes in Medical Applications. *Materials* **2021**, *14*, 191. [[CrossRef](#)] [[PubMed](#)]
32. Tofail, S.A.; Koumoulos, E.P.; Bandyopadhyay, A. Additive manufacturing: Scientific and technological challenges, market uptake and opportunities. *Mater. Today* **2018**, *21*, 22–37. [[CrossRef](#)]
33. Froes, F.; Dutta, B. The Additive Manufacturing (AM) of Titanium Alloys. *Adv. Mater. Res.* **2014**, *1019*, 19–25. [[CrossRef](#)]
34. Zeng, M.; Zavanelli, D.; Chen, J.; Saeidi-Javash, M.; Du, Y.; LeBlanc, S.; Snyder, G.J.; Zhang, Y. Printing thermoelectric inks toward next-generation energy and thermal devices. *Chem. Soc. Rev.* **2021**, *51*, 485–512. [[CrossRef](#)]
35. Orrill, M.; LeBlanc, S. Printed thermoelectric materials and devices: Fabrication techniques, advantages, and challenges. *J. Appl. Polym. Sci.* **2017**, *134*. [[CrossRef](#)]
36. Masoumi, S.; O'Shaughnessy, S.; Pakdel, A. Organic-based flexible thermoelectric generators: From materials to devices. *Nano Energy* **2021**, *92*, 106774. [[CrossRef](#)]
37. Tian, Y.; Molina-Lopez, F. Boosting the performance of printed thermoelectric materials by inducing morphological anisotropy. *Nanoscale* **2021**, *13*, 5202–5215. [[CrossRef](#)] [[PubMed](#)]
38. Daminabo, S.C.; Goel, S.; Grammatikos, S.A.; Nezhad, H.Y.; Thakur, V.K. Fused deposition modeling-based additive manufacturing (3D printing): Techniques for polymer material systems. *Mater. Today Chem.* **2020**, *16*, 100248. [[CrossRef](#)]
39. Wang, J.; Li, H.; Liu, R. Thermoelectric and mechanical properties of PLA/Bi<sub>0.5</sub>Sb<sub>1.5</sub>Te<sub>3</sub> composite wires used for 3D printing. *Compos. Sci. Technol.* **2018**, *157*, 1–9. [[CrossRef](#)]
40. Oztan, C.; Ballikaya, S.; Ozgun, U.; Karkkainen, R.; Celik, E. Additive manufacturing of thermoelectric materials via fused filament fabrication. *Appl. Mater. Today* **2019**, *15*, 77–82. [[CrossRef](#)]
41. Aw, Y.Y.; Yeoh, C.K.; Idris, M.A.; Teh, P.L.; Hamzah, K.A.; Szali, S.A. Effect of Printing Parameters on Tensile, Dynamic Mechanical, and Thermoelectric Properties of FDM 3D Printed CABS/ZnO Composites. *Materials* **2018**, *11*, 466. [[CrossRef](#)] [[PubMed](#)]

42. Cho, C.; Stevens, B.; Hsu, J.-H.; Bureau, R.; Hagen, D.A.; Regev, O.; Yu, C.; Grunlan, J.C. Completely Organic Multilayer Thin Film with Thermoelectric Power Factor Rivaling Inorganic Tellurides. *Adv. Mater.* **2015**, *27*, 2996–3001. [[CrossRef](#)] [[PubMed](#)]
43. Kim, F.; Kwon, B.; Eom, Y.; Lee, J.E.; Park, S.; Jo, S.; Park, S.H.; Kim, B.-S.; Im, H.J.; Lee, M.H.; et al. 3D printing of shape-conformable thermoelectric materials using all-inorganic Bi<sub>2</sub>Te<sub>3</sub>-based inks. *Nat. Energy* **2018**, *3*, 301–309. [[CrossRef](#)]
44. Lee, J.; Choo, S.; Ju, H.; Hong, J.; Yang, S.E.; Kim, F.; Gu, D.H.; Jang, J.; Kim, G.; Ahn, S.; et al. Doping-Induced Viscoelasticity in PbTe Thermoelectric Inks for 3D Printing of Power-Generating Tubes. *Adv. Energy Mater.* **2021**, *11*, 2100190. [[CrossRef](#)]
45. Rocha, V.G.; Saiz, E.; Tirichenko, I.S.; García-Tuñón, E. Direct ink writing advances in multi-material structures for a sustainable future. *J. Mater. Chem. A* **2020**, *8*, 15646–15657. [[CrossRef](#)]
46. Yang, S.E.; Kim, F.; Ejaz, F.; Lee, G.S.; Ju, H.; Choo, S.; Lee, J.; Kim, G.; Jung, S.-H.; Ahn, S.; et al. Composition-segmented BiSbTe thermoelectric generator fabricated by multimaterial 3D printing. *Nano Energy* **2020**, *81*, 105638. [[CrossRef](#)]
47. Choo, S.; Ejaz, F.; Ju, H.; Kim, F.; Lee, J.; Yang, S.E.; Kim, G.; Kim, H.; Jo, S.; Baek, S.; et al. Cu<sub>2</sub>Se-based thermoelectric cellular architectures for efficient and durable power generation. *Nat. Commun.* **2021**, *12*, 1–11. [[CrossRef](#)] [[PubMed](#)]
48. Tran, T.S.; Dutta, N.K.; Choudhury, N.R. Graphene inks for printed flexible electronics: Graphene dispersions, ink formulations, printing techniques and applications. *Adv. Colloid Interface Sci.* **2018**, *261*, 41–61. [[CrossRef](#)] [[PubMed](#)]
49. Michael, G.B.; MarkáRodger, P. Inhibition of crystal growth in methane hydrate. *J. Chem. Soc. Faraday Trans.* **1995**, *91*, 3449–3460.
50. Wang, M.; Bai, J.; Shao, K.; Tang, W.; Zhao, X.; Lin, D.; Huang, S.; Chen, C.; Ding, Z.; Ye, J. Poly(vinyl alcohol) Hydrogels: The Old and New Functional Materials. *Int. J. Polym. Sci.* **2021**, *2021*, 1–16. [[CrossRef](#)]
51. Su, N.; Zhu, P.; Pan, Y.; Li, F.; Li, B. 3D-printing of shape-controllable thermoelectric devices with enhanced output performance. *Energy* **2020**, *195*, 116892. [[CrossRef](#)]
52. Kenel, C.; Al Malki, M.; Dunand, D. Microstructure evolution during reduction and sintering of 3D-extrusion-printed Bi<sub>2</sub>O<sub>3</sub>+TeO<sub>2</sub> inks to form Bi<sub>2</sub>Te<sub>3</sub>. *Acta Mater.* **2021**, *221*, 117422. [[CrossRef](#)]
53. Horst, T.A.; Rottengruber, H.; Seifert, M.; Ringler, J. Dynamic heat exchanger model for performance prediction and control system design of automotive waste heat recovery systems. *Appl. Energy* **2013**, *105*, 293–303. [[CrossRef](#)]
54. Dai, D.; Zhou, Y.; Liu, J. Liquid metal based thermoelectric generation system for waste heat recovery. *Renew. Energy* **2011**, *36*, 3530–3536. [[CrossRef](#)]
55. Su, Q.; Chang, S.; Zhao, Y.; Zheng, H.; Dang, C. A review of loop heat pipes for aircraft anti-icing applications. *Appl. Therm. Eng.* **2018**, *130*, 528–540. [[CrossRef](#)]
56. Garofalo, E.; Bevione, M.; Cecchini, L. Waste heat to power: Technologies, current applications, and future potential. *Energy Technol.* **2020**, *8*, 2000413. [[CrossRef](#)]
57. Asif, S.; Chansoria, P.; Shirwaiker, R. Ultrasound-assisted vat photopolymerization 3D printing of preferentially organized carbon fiber reinforced polymer composites. *J. Manuf. Process.* **2020**, *56*, 1340–1343. [[CrossRef](#)]
58. Davoudinejad, A. Vat photopolymerization methods in additive manufacturing. In *Additive Manufacturing*; Elsevier: Amsterdam, The Netherlands, 2021; pp. 159–181.
59. He, M.; Zhao, Y.; Wang, B.; Xi, Q.; Zhou, J.; Liang, Z. 3D printing fabrication of amorphous thermoelectric materials with ultralow thermal conductivity. *Small* **2015**, *11*, 5889–5894. [[CrossRef](#)] [[PubMed](#)]
60. Park, D.; Lee, S.; Kim, J. Thermoelectric and mechanical properties of PEDOT: PSS-coated Ag<sub>2</sub>Se nanowire composite fabricated via digital light processing based 3D printing. *Compos. Commun.* **2022**, *30*, 101084. [[CrossRef](#)]
61. Ferhat, M.; Nagao, J. Thermoelectric and transport properties of β-Ag<sub>2</sub>Se compounds. *J. Appl. Phys.* **2000**, *88*, 813–816. [[CrossRef](#)]
62. Park, D.; Lee, S.; Kim, J. Enhanced thermoelectric performance of UV-curable silver (I) selenide-based composite for energy harvesting. *Sci. Rep.* **2021**, *11*, 16683. [[CrossRef](#)] [[PubMed](#)]
63. Medellin, A.; Du, W.; Miao, G.; Zou, J.; Pei, Z.; Ma, C. Vat Photopolymerization 3D Printing of Nanocomposites: A Literature Review. *J. Micro Nano-Manuf.* **2019**, *7*, 031006. [[CrossRef](#)]
64. Lou, S.; Jiang, X.; Sun, W.; Zeng, W.; Pagani, L.; Scott, P. Characterisation methods for powder bed fusion processed surface topography. *Precis. Eng.* **2018**, *57*, 1–15. [[CrossRef](#)]
65. Mueller, B. Additive manufacturing technologies—rapid prototyping to direct digital manufacturing. *Assem. Autom.* **2012**, *32*. [[CrossRef](#)]
66. Chueh, Y.-H.; Zhang, X.; Ke, J.C.-R.; Li, Q.; Wei, C.; Li, L. Additive manufacturing of hybrid metal/polymer objects via multiple-material laser powder bed fusion. *Addit. Manuf.* **2020**, *36*, 101465. [[CrossRef](#)]
67. Sorrentino, R.; Peverini, O.A. Additive manufacturing: A key enabling technology for next-generation microwave and millimeter-wave systems [point of view]. *Proc. IEEE* **2016**, *104*, 1362–1366. [[CrossRef](#)]
68. Takaichi, A.; Suyalatu; Nakamoto, T.; Joko, N. Microstructures and mechanical properties of Co–29Cr–6Mo alloy fabricated by selective laser melting process for dental applications. *J. Mech. Behav. Biomed. Mater.* **2013**, *21*, 67–76. [[CrossRef](#)] [[PubMed](#)]
69. Bertoli, U.S. *Process-Structure-Properties Relationships in Laser Powder Bed Fusion Additive Manufacturing*; University of California: Irvine, CA, USA, 2018.
70. Van Elsen, M.; Al-Bender, F.; Kruth, J. Application of dimensional analysis to selective laser melting. *Rapid Prototyp. J.* **2008**, *14*, 15–22. [[CrossRef](#)]
71. Mukherjee, T.; Manvatkar, V.; De, A.; Debroy, T. Dimensionless numbers in additive manufacturing. *J. Appl. Phys.* **2017**, *121*, 064904. [[CrossRef](#)]

72. Gomell, L.; Roscher, M.; Bishara, H.; Jäggle, E.A.; Scheu, C.; Gault, B. Properties and influence of microstructure and crystal defects in Fe<sub>2</sub>VAl modified by laser surface remelting. *Scr. Mater.* **2020**, *193*, 153–157. [[CrossRef](#)]
73. Feng, B.; Li, G.; Hu, X. Improvement of thermoelectric and mechanical properties of BiCuSeO-based materials by SiC nanodispersion. *J. Alloy. Compd.* **2020**, *818*, 152899. [[CrossRef](#)]
74. Read, A.L. *Selective Laser Melting Parameters for Use in the Manufacture of Thermoelectric Materials*; The George Washington University: Washington, DC, USA, 2015.
75. El-Desouky, A.; Read, A.L.; Bardet, P.M. Selective laser melting of a bismuth telluride thermoelectric materials. In Proceedings of the Solid Free Symp, Solid Freeform Fabrication Symposium, Austin, TX, USA, 10–12 August 2015; pp. 1043–1050.
76. El-Desouky, A.; Carter, M.; Andre, M.A.; Bardet, P.M.; LeBlanc, S. Rapid processing and assembly of semiconductor thermoelectric materials for energy conversion devices. *Mater. Lett.* **2016**, *185*, 598–602. [[CrossRef](#)]
77. El-Desouky, A.; Carter, M.; Mahmoudi, M.; Elwany, A.; LeBlanc, S. Influences of energy density on microstructure and consolidation of selective laser melted bismuth telluride thermoelectric powder. *J. Manuf. Process.* **2017**, *25*, 411–417. [[CrossRef](#)]
78. Zhang, H.; Hobbis, D.; Nolas, G.S.; LeBlanc, S. Laser additive manufacturing of powdered bismuth telluride. *J. Mater. Res.* **2018**, *33*, 4031–4039. [[CrossRef](#)]
79. Welch, R.; Hobbis, D.; Nolas, G.; Leblanc, S. Meso-, micro-, and nano-structures induced in bismuth telluride thermoelectric materials by laser additive manufacturing. In *Energy Harvesting and Storage: Materials, Devices, and Applications X*; International Society for Optics and Photonics: Washington, DC, USA, 2020; Volume 11387, p. 1138710. [[CrossRef](#)]
80. Welch, R.; Hobbis, D.; Birnbaum, A.J. Nano-and Micro-Structures Formed during Laser Processing of Selenium Doped Bismuth Telluride. *Adv. Mater. Interfaces* **2021**, *8*, 2100185. [[CrossRef](#)]
81. Zhang, H.; Wang, S.; Taylor, P.J.; Yang, J.; LeBlanc, S. Selective laser melting of half-Heusler thermoelectric materials. In *Energy Harvesting and Storage: Materials, Devices, and Applications VIII*; International Society for Optics and Photonics: Bellingham, WA, USA, 2018; Volume 10663, p. 106630B.
82. Thimont, Y.; Presmanes, L.; Baylac, V.; Tailhades, P.; Berthebaud, D.; Gascoin, F. Thermoelectric Higher Manganese Silicide: Synthesized, sintered and shaped simultaneously by selective laser sintering/Melting additive manufacturing technique. *Mater. Lett.* **2018**, *214*, 236–239. [[CrossRef](#)]
83. Shi, J.; Chen, X.; Wang, W.; Chen, H. A new rapid synthesis of thermoelectric Sb<sub>2</sub>Te<sub>3</sub> ingots using selective laser melting 3D printing. *Mater. Sci. Semicond. Process.* **2020**, *123*, 105551. [[CrossRef](#)]
84. Clare, A.T.; Chalker, P.R.; Davies, S.; Sutcliffe, C.J.; Tsopanos, S. Selective laser sintering of barium titanate–polymer composite films. *J. Mater. Sci.* **2008**, *43*, 3197–3202. [[CrossRef](#)]
85. Dong, Y.; Jiang, H.; Chen, A.; Yang, T.; Zou, T.; Xu, D. Porous Al<sub>2</sub>O<sub>3</sub> ceramics with spontaneously formed pores and enhanced strength prepared by indirect selective laser sintering combined with reaction bonding. *Ceram. Int.* **2020**, *46*, 15159–15166. [[CrossRef](#)]
86. Xiong, X.; Zhu, L.; Wang, G.; Liu, D.; Zhang, Q.; Feng, W. Microstructure and properties of n-type Bi<sub>2</sub>Te<sub>3</sub>-based thermoelectric material fabricated by selective laser sintering. *Mater. Res. Express* **2020**, *7*, 066504. [[CrossRef](#)]
87. Qiu, J.; Yan, Y.; Luo, T.; Tang, K.; Yao, L.; Zhang, J.; Zhang, M.; Su, X.; Tan, G.; Xie, H.; et al. 3D Printing of highly textured bulk thermoelectric materials: Mechanically robust BiSbTe alloys with superior performance. *Energy Environ. Sci.* **2019**, *12*, 3106–3117. [[CrossRef](#)]
88. Wu, K.; Yan, Y.; Zhang, J.; Mao, Y.; Xie, H.; Yang, J.; Zhang, Q.; Uher, C.; Tang, X. Preparation of n-type Bi<sub>2</sub>Te<sub>3</sub> thermoelectric materials by non-contact dispenser printing combined with selective laser melting. *Phys. Status solidi (RRL)–Rapid Res. Lett.* **2017**, *11*, 1700067. [[CrossRef](#)]
89. Mao, Y.; Yan, Y.; Wu, K.; Xie, H.; Xiu, Z.; Yang, J.; Zhang, Q.; Uher, C.; Tang, X. Non-equilibrium synthesis and characterization of n-type Bi<sub>2</sub>Te<sub>2.7</sub>Se<sub>0.3</sub> thermoelectric material prepared by rapid laser melting and solidification. *RSC Adv.* **2017**, *7*, 21439–21445. [[CrossRef](#)]
90. Greifzu, M.; Tkachov, R.; Stepien, L.; López, E.; Brückner, F.; Leyens, C. Laser Treatment as Sintering Process for Dispenser Printed Bismuth Telluride Based Paste. *Materials* **2019**, *12*, 3453. [[CrossRef](#)]
91. Yan, Y.; Ke, H.; Yang, J. Fabrication and thermoelectric properties of n-type CoSb<sub>2.85</sub>Te<sub>0.15</sub> using selective laser melting. *ACS Appl. Mater. Interfaces* **2018**, *10*, 13669–13674. [[CrossRef](#)]
92. Yan, Y.; Geng, W.; Qiu, J.; Ke, H.; Luo, C.; Yang, J.; Uher, C.; Tang, X. Thermoelectric properties of n-type ZrNiSn prepared by rapid non-equilibrium laser processing. *RSC Adv.* **2018**, *8*, 15796–15803. [[CrossRef](#)]
93. Chen, T.-L.; Luo, C.; Yan, Y.-G.; Yang, J.-H.; Zhang, Q.-J.; Uher, C.; Tang, X.-F. Rapid fabrication and thermoelectric performance of SnTe via non-equilibrium laser 3D printing. *Rare Met.* **2018**, *37*, 300–307. [[CrossRef](#)]
94. Murr, L.E.; Martinez, E.; Gaytan, S.M.; Ramirez, D.A.; Machado, B.I.; Shindo, P.W.; Martinez, J.L.; Medina, F.; Wooten, J.; Ciscel, D.; et al. Microstructural Architecture, Microstructures, and Mechanical Properties for a Nickel-Base Superalloy Fabricated by Electron Beam Melting. *Met. Mater. Trans. A* **2011**, *42*, 3491–3508. [[CrossRef](#)]
95. Li, G.; An, Q.; Li, W.; Goddard, I.W.A.; Zhai, P.; Zhang, Q.; Snyder, G.J. Brittle Failure Mechanism in Thermoelectric Skutterudite CoSb<sub>3</sub>. *Chem. Mater.* **2015**, *27*, 6329–6336. [[CrossRef](#)]
96. Li, G.; An, Q.; Goddard, W.A., III. Atomistic explanation of brittle failure of thermoelectric skutterudite CoSb<sub>3</sub>. *Acta Mater.* **2016**, *103*, 775–780. [[CrossRef](#)]

97. Pei, W.; Zhengying, W.; Zhen, C.; Junfeng, L.; Shuzhe, Z.; Jun, D. Numerical simulation and parametric analysis of selective laser melting process of AlSi10Mg powder. *Appl. Phys. A* **2017**, *123*, 540. [[CrossRef](#)]
98. Li, Y.; Gu, D. Thermal behavior during selective laser melting of commercially pure titanium powder: Numerical simulation and experimental study. *Addit. Manuf.* **2014**, *1*, 99–109. [[CrossRef](#)]
99. Khan, M.; Sheikh, N.A.; Jaffery, S. Numerical simulation of melt pool instability in the selective laser melting (slm) process. *Lasers Eng.* **2014**, *28*, 319–336.
100. Ansari, P.; Salamci, M.U. On the selective laser melting based additive manufacturing of AlSi10Mg: The process parameter investigation through multiphysics simulation and experimental validation. *J. Alloy. Compd.* **2021**, *890*, 161873. [[CrossRef](#)]
101. Leitz, K.-H.; Singer, P.; Plankensteiner, A.; Tabernig, B.; Kestler, H.; Sigl, L. Multi-physical simulation of selective laser melting. *Met. Powder Rep.* **2017**, *72*, 331–338. [[CrossRef](#)]
102. Yuan, P.; Gu, D. Molten pool behaviour and its physical mechanism during selective laser melting of TiC/AlSi10Mg nanocomposites: Simulation and experiments. *J. Phys. D Appl. Phys.* **2015**, *48*, 035303. [[CrossRef](#)]
103. Tang, Q.; Chen, P.; Chen, J.; Chen, Y.; Chen, H. Numerical simulation of selective laser melting temperature conduction behavior of H13 steel in different models. *Optik* **2019**, *201*, 163336. [[CrossRef](#)]
104. King, W.; Anderson, A.T.; Ferencz, R.M.; Hodge, N.E.; Kamath, C.; Khairallah, S.A. Overview of modelling and simulation of metal powder bed fusion process at Lawrence Livermore National Laboratory. *Mater. Sci. Technol.* **2015**, *31*, 957–968. [[CrossRef](#)]